CrystEngComm

PAPER

View Article Online
View Journal | View Issue

Check for updates

Cite this: *CrystEngComm*, 2020, **22**, 5743

Epitactic growth of celestite on anhydrite: substrate induced twinning and morphological evolution of aggregates†

Pablo Forjanes, *[a] Juan Gómez-Barreiro, [b] Juan Morales, [b] José Manuel Astilleros [ac] and Lurdes Fernández-Díaz [ac]

Received 22nd May 2020,
Accepted 8th August 2020

DOI: 10.1039/d0ce00755b

rsc.li/crystengcomm

Epitactic crystal growth plays a main role in the development of mineral processes and in the synthesis of advanced materials. Celestite ($SrSO_4$) forms epitactic overgrowths on anhydrite ($CaSO_4$) (100), (010) and (001) surfaces upon interacting with Sr-bearing aqueous solutions. Two populations of differently oriented celestite crystals related by symmetry operators of substrate are identified on $(001)_{Anh}$ and $(100)_{Anh}$ anhydrite substrates by SEM observations and synchrotron X-ray diffraction analysis. Substrate-induced twins arise after the coalescence of individuals belonging to these populations. Progressing growth results in a marked morphological evolution of epitactic celestite, whose crystals undergo sustained branching and loss of co-orientation that result in the formation of sheaf-like aggregates, on $(100)_{Anh}$, and swan-like aggregates, on $(001)_{Anh}$. We relate this evolution to celestite growth in a Ca-rich environment due to continued anhydrite dissolution and incorporation of small amounts of Ca into celestite structure. This incorporation would induce lattice strain which would be released through the formation of dislocations. The regular arrangement of these dislocations in small-angle boundaries would result in progressive splitting, driving the evolution from celestite single crystals to aggregates. Sharp compositional gradients in the boundary layer could explain the anisotropic development that leads to the formation of the swan-like celestites.

Introduction

Epitactic growth is a main step in the processes of synthesis of a variety of materials for industrial applications, from electronics to semiconductors.[1,2] Epitactic growth is also a common phenomenon in natural environments. Indeed, the existence of structural similarities between mineral crystals facilitates their transformation into one another. This is particularly so for polymorphic reconstructive phase transitions, whose kinetics significantly accelerates when they have a topotactic character.[3–10] In contrast, the formation of epitactic layers often hinders the development of the interface coupled dissolution–crystallization reactions, which control mineral pseudomorphic replacements in numerous geological setups.[11–14] Indeed, even the formation of a nanometric epitactic layer of a secondary phase on a mineral surface that interacts with a fluid phase can effectively armor the mineral substrate. An early armoring can partially or fully prevent the progress of the mineral surface–fluid interaction, thereby, leading to the slowdown or even the complete stoppage of the dissolution–crystallization reaction.[12,13,15] The effectiveness of the epitactic growth-related hindering of a dissolution–crystallization reaction strongly depends on the characteristics of the overgrown epitactic layer.[16] These characteristics are defined by the goodness of the structural matching between the overgrowth and the substrate phase through their interface.[17] The quality of the structural fitting determines the epitactic growth mechanism involved in the formation of the overgrowth and defines the degree of substrate–overgrowth interface coherency and adhesion.[17] Epitactic growth that involves low interface misfits occurs through the Frank–Van der Merwe mechanism and is commonly characterized by coherent interfaces and high substrate–overgrowth adhesions.[18,19] In contrast, higher interface misfits lead to epitactic growth dominated by the Stranski–Krastanov or the Volmer–Weber mechanisms and result in the formation of epitactic layers with poor substrate–overgrowth adhesion and semi to incoherent interfaces.[1,16,20–23] Frank–Van der Merwe epitactic layers provide a significantly better armoring of a substrate than

---

[a] *Departamento de Mineralogía y Petrología, Universidad Complutense de Madrid, 28040, Madrid, Spain. E-mail: pforjane@ucm.es*
[b] *Departamento de Geología, Universidad de Salamanca, 37008, Salamanca, Spain*
[c] *Instituto de Geociencias (IGEO), (UCM, CSIC), 28040, Madrid, Spain*

† Electronic supplementary information (ESI) available. See DOI: 10.1039/d0ce00755b

those epitactic layers that form through the Stranski–Krastanov or the Volmer–Weber mechanisms because the latter layers contain a certain volume of intrinsic microporosity. This microporosity constitutes a permanent path for the communication between the bulk growth medium and the overgrowth–substrate interface.[16,23] The quality of the armoring provided by an epitactic layer can decrease as the thickness of the overgrowth increases and lattice-mismatch strain accumulates.[24] This strain will eventually be relaxed through the formation of dislocations,[25–27] as is, for example, observed during the preparation of heteroepitaxial semiconductor films.[28–30] Strain dislocations represent an intrinsic source of misorientation that drives the progressive polygonization of epitactic layers and negatively affects the armouring of the substrate that these layers provide. Polygonization and progressive loss of co-alignment within an epitactic layer can also result from external factors like the incorporation of impurities into the structure of the overgrowth since it also induces lattice strain and eventually can lead to the nucleation of dislocations and the polygonization of the overgrowth.[24,25,31,32] In geological environments, where crystal growth commonly occurs in chemically complex systems, the growth of impurity-bearing mineral phases is the norm,[33,34] as most minerals grow as solid solutions that show a variety of chemical zoning patterns.[25,35–37] The effect of impurity incorporation on the evolution of orientational features within mineral overgrowths that form during dissolution–crystallization reactions may significantly affect the kinetics of the mineral transformations that take place in these settings.

Celestite ($SrSO_4$) is the main ore of strontium.[38] Strontium has been widely used in different industries,[38] including ferrites production, fabrication pyrotechnics, cathode-ray tubes and in drilling muds, substituting Ba, when prices for this element shoot up. All large exploitable deposits of celestite are associated to sedimentary rocks, where they are spatially and genetically associated to carbonate and sulphate evaporitic formations.[39] The formation of celestite deposits has been related to the interaction of calcium sulphate minerals, namely gypsum ($CaSO_4·2H_2O$) and/or ($CaSO_4$) anhydrite, with Sr-rich fluids.[39] This interaction would result in the release of sulphate ions to the fluid phase through the dissolution of the calcium sulphate mineral, which would be immediately followed by the precipitation of celestite.[39,40] The existence of a during time-sustained feedback loop between the dissolution and precipitation reactions could explain the large volumes of celestite deposits in these geological settings. Here, we study the formation of celestite on the three main cleavage surfaces of anhydrite, (100), (010) and (001), upon their interaction with Sr-bearing aqueous solutions. Celestite initially grows oriented on all anhydrite cleavage surfaces. However, a progressive loss of co-orientation is observed as celestite growth progresses. We describe the epitactic relationships between celestite and anhydrite substrates as well as the evolution of celestite crystal morphology and the associated progressive loss of co-orientation during growth. By combining morphological observations and crystallographic and chemical analyses we aim to advance in the understanding of the factors that control the evolution of orientational features within epitactic overgrowths in natural multicomponent systems and evaluate its possible influence in the kinetics of mineral transformation that take place through dissolution–crystallization reactions.

Experimental

We conducted interaction experiments between anhydrite ($CaSO_4$) surfaces and Sr-bearing aqueous solutions ($[Sr]_{aq}$ = 0, 0.1, 1.0, 10 and 50 g L^{-1}) at 25 °C ± 0.5 °C and atmospheric pressure. The Sr-bearing aqueous solutions were prepared by dissolving reagent-grade $SrCl_2·6H_2O$ in high purity deionized water (MiliQ) (18 MΩ cm). The anhydrite samples were 1 mm thick, square-shaped (3 × 3 mm^2) slices of highly pure blue single crystals from Naica (Chihuahua, México). These slices were cut parallel to the (001), (010) and (100) planes. Their orientation with respect to the main crystallographic directions of anhydrite was confirmed by observing their interference figure using a polarized optical microscope.

Freshly cleaved anhydrite slices were placed in glass reactors, laying on one of their squared surfaces. The reactors were then filled with 5 ml of the Sr-bearing aqueous solution and sealed with a polystyrene cap. The experiments were finished after set interaction times (30 minutes; 1, 2 and 6 hours; 1, 5, 7, 14 and 20 days). Independent runs were conducted for each of the three cleavage surfaces and each time of interaction considered. After finishing the experiments, the anhydrite samples were removed from the Sr-bearing solutions, thoroughly rinsed with MiliQ water and left to dry overnight at 45 °C in a thermostatic chamber. Afterwards, anhydrite samples were mounted on holders, with their larger surface that had been exposed to the Sr-bearing solution lying upwards. New phases formed on anhydrite surfaces were analyzed by glancing incidence X-ray diffraction (GIXRD) using a Philips X'Pert PRO MRD diffractometer equipped with a Cu-Kα source (45 kV, 40 mA), a X-ray parabolic mirror in the incident beam and a parallel plate collimator with flat graphite monochromator in the diffracted beam (Xe proportional detector). The surfaces were scanned over the range 2θ = 20–90° at a scan speed of 0.8° min^{-1} and with a 0.1° beam incidence angle. Standard mineral files for celestite (COD-96-900-4091)[41] and anhydrite (COD-96-900-4096)[42] of the Crystallographic Open Database (COD, 2017 version) and glancing incidence X-ray diffraction diagrams were correlated to determine solid phases. Anhydrite samples were then coated, first with carbon (Quorum Q150T-E; 8 nm) and then with gold (Quorum Q150R-S; 15 nm), and studied by means of a scanning electron microscope (JEOL JSM 6400, 40 kV) to obtain information on dissolution features and morphological characteristics of precipitates newly formed on anhydrite surfaces as a result of its interaction with the Sr-bearing aqueous solutions. Cross sections of some of the anhydrite samples were also prepared by embedding them in epoxy resin and polishing down to the middle of the crystals. Backscattered scanning electron microscope (BSEM) imaging of these cross-sections allowed for the identification of different phases on the basis of their difference in contrast. The scanning electron microscope was equipped with an energy dispersive spectrometer (LINK Ex1; Oxford Instruments 80 mm^2 X-Max SDD; acquisition time: 120 seconds) that allowed to obtain information on chemical characteristics of the newly formed phases. Most EDX analysis were collected in the embedded samples to avoid any possible influence coming from the anhydrite substrate.

The shape of the newly formed crystals was modelled using the JCrystal software (KrystalShaper, 2019). Finally, structure computer models were constructed using the CrystalMaker software for analysing the crystallographic relationships between anhydrite surfaces and the newly formed precipitates.[43]

Synchrotron diffraction experiments

Cleaved slices of anhydrite were prepared as described in the previous section to explore the epitactic growth of celestite on (100), (010) and (001) anhydrite substrates through synchrotron diffraction experiments. After the interaction with the Sr-bearing solutions, the samples were mounted on a goniometer with a glass pin for rotation. The experimental reference system is shown in Fig. 1, where the rotation axis ($\omega//Y$) is parallel to anhydrite [001], [100] and [100] for (100), (010) and (001) anhydrite slices, respectively. The diffraction experiments were done at the ID11 beamline at the European Synchrotron Radiation Facility (ESRF), France.[44] The experimental setup and procedure were as follows. A monochromatic X-rays beam (dimensions 0.5 × 0.5 mm; wavelength 0.030996 nm) was directed at the sample, previously mounted on a goniometer head and investigated in transmission geometry. Diffraction images were recorded by a FreLoN detector (2048 × 2048 pixels), 23 cm away from the sample.

Diffraction images display Debye rings with azimuthal intensity variations indicating texture, and very bright single crystal diffraction spots (Fig. 2). Both patterns have been indexed by correlating diffraction diagrams and standard mineral files of the Crystallographic Open Database (COD, 2017 version) matching celestite and anhydrite standard patterns, respectively (Fig. 2).

During data collection, in order to prevent the detector saturation, 60 images were collected with a short acquisition time (0.5 s) for each sample. In order to improve pole figure coverage, the sample slice was rotated around an axis perpendicular to the beam ($\omega//Y$; Fig. 1) from +10° to −10°. A CeO_2 standard was measured in the same conditions as the samples to determine instrumental parameters, like sample to detector distance.

Diffraction images from each rotation were corrected for FReLon geometrical distortion and merged into a single image in TIFF format, using Fit2D software.[45] Images were decomposed with the Rietveld program MAUD (Material Analysis Using Diffraction)[46] into 72 azimuthal sectors of 5°, over which intensity was integrated, providing a total of 216 diffraction spectra per sample (Fig. 2). In some cases, the severe overlapping of the anhydrite single crystal pattern prevented the use of some sectors, which were manually eliminated from the dataset. In the Rietveld refinement, the celestite crystal structure by Hawthorne and Ferguson[41] ($Pnma$; a = 8.360 Å, b = 5.352 Å, c = 6.858 Å) was used as reference.

For quantitative texture analysis, E-WIMV algorithm[47] was applied, as implemented in MAUD, without imposing any sample symmetry. The final celestite orientation distributions (OD) were exported to BEARTEX for additional processing and recalculation of pole figures.[48] Texture strength is quantified in pole-figures density scale (multiples of a random distribution, m.r.d.) and F^2 index.[49] A detailed description of the method is published elsewhere.[49–53]

Results

SEM imaging of freshly cleaved anhydrite (001), (010) and (100) surfaces shows that they consist of large flat terraces

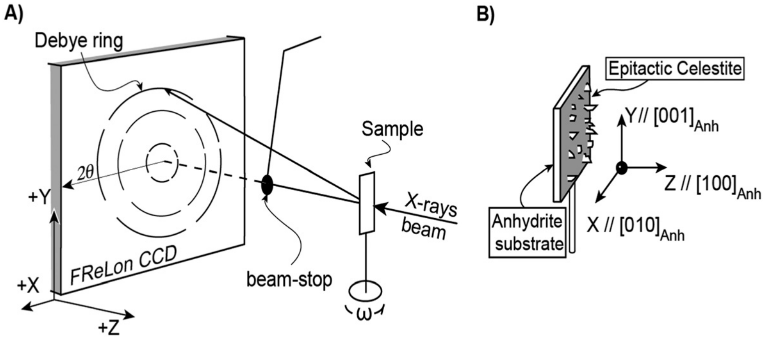

Fig. 1 Experimental (A) and sample (B) reference system. Coordinate system for anhydrite (100) sample is described in (B) as an example. For anhydrite (001) and (010), $Y//[100]_{\mathrm{Anh}} - X//[010]_{\mathrm{Anh}}$, and $Y//[100]_{\mathrm{Anh}} - X//[001]_{\mathrm{Anh}}$, respectively. See the text for a discussion.

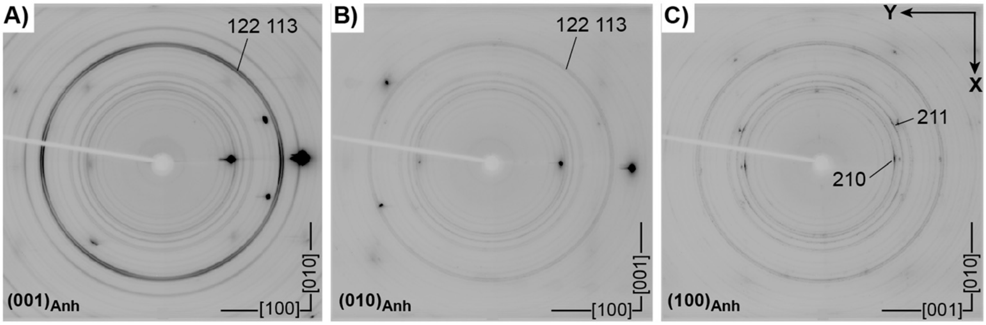

Fig. 2 Diffraction images with Debye rings (celestite) and spots (anhydrite), for the three different substrate orientations studied: (A) anhydrite (001), (B) anhydrite (010) and (C) anhydrite (100). Intensity variations along Debye rings are due to celestite texture. Some planes are indexed. Reference system (*XYZ*) as defined in Fig. 1.

bounded by macrosteps. Slightly different features are observed on the (001) surface, which appears rougher and contains a larger number of steps than the other two surfaces. In all cases, after 30 minutes of interaction of the anhydrite substrates with either pure water or an aqueous solution bearing Sr, the formation of etch-pits on flat terraces is observed. The characteristics of these etch-pits on an anhydrite (100) surface after its interaction with water are depicted in Fig. 3a (interaction time 30 minutes). The progress of the interaction latter leads to the nucleation of a secondary phase on the anhydrite surfaces considered when $[\mathrm{Sr}]_{\mathrm{aq}} \geq 1\ \mathrm{g\ L^{-1}}$ (Fig. 3b). Regardless of the interaction time no new phase is observed to form on any anhydrite cleavage surface when the interaction takes place with aqueous solutions containing $[\mathrm{Sr}]_{\mathrm{aq}} < 1\ \mathrm{g\ L^{-1}}$ (Fig. S1†).

Several EDX spectra were collected in epoxy-embedded cross-cut sections of anhydrite crystals interacted with a $[\mathrm{Sr}]_{\mathrm{aq}} = 50\ \mathrm{g\ L^{-1}}$ for 7 days (Fig. 3c and S2†). EDX spectrums portrayed on the new phase show that these crystals primarily consist of oxygen, sulfur and strontium, with small contents of calcium (up to 1.5 wt% in almost every analysis; detection limit of the EDX is approximately 0.1 wt% for bulk materials). These EDX analyses support that these new crystals are Ca-bearing celestite. Most analyses were portrayed in cross-cut sections to avoid any possible influence coming from the anhydrite substrate. Additional EDX spectra collected on celestite crystals grown on all anhydrite substrates considered after their interaction with aqueous solutions bearing $[\mathrm{Sr}]_{\mathrm{aq}} \geq 1\ \mathrm{g\ L^{-1}}$ show similar characteristics. This interpretation is further supported by the results of GIXRD analysis. A GIXRD diagram taken on an anhydrite (001) cleavage surface after 2 hours interaction with a $[\mathrm{Sr}]_{\mathrm{aq}} = 50\ \mathrm{g\ L^{-1}}$ is shown in Fig. 3d. All diffraction peaks match well those of celestite, although some of them appear slightly shifted towards higher 2θ angles compared to their positions in the standard XRD pattern of celestite (COD-96-900-4091).[41]

The substrate surface area carpeted by celestite crystals progressively increases and celestite crystal growth and coalescence leads to the formation of a layer that appears patchy when the interaction occurs with an aqueous solution with $[\mathrm{Sr}]_{\mathrm{aq}} = 1\ \mathrm{g\ L^{-1}}$ regardless of both, the anhydrite substrate and the interaction time considered. When the interaction takes place with aqueous solutions with higher Sr concentrations ($[\mathrm{Sr}]_{\mathrm{aq}} \geq 10\ \mathrm{g\ L^{-1}}$) this layer becomes continuous after an interaction time that varies depending on both, the specific initial $[\mathrm{Sr}]_{\mathrm{aq}}$ value in the aqueous solution and the orientation of the anhydrite substrate (Fig. 4a and S3†). Thus, after two hours interaction with a $[\mathrm{Sr}]_{\mathrm{aq}} = 50\ \mathrm{g\ L^{-1}}$, 80% of the anhydrite (001) substrate is already carpeted by celestite crystals. This percentage decreases to less than 50% in the case of anhydrite (010) and (100) substrates (Fig. S4†). On anhydrite (001) surface celestite crystals already form a continuous layer after only one day of interaction while anhydrite (100) and (010) surfaces only appear completely carpeted by a continuous celestite layer after three days interaction with an aqueous solution bearing $[\mathrm{Sr}]_{\mathrm{aq}} = 50\ \mathrm{g\ L^{-1}}$. The interaction time for the formation of a continuous layer when the aqueous solution contains $[\mathrm{Sr}]_{\mathrm{aq}} = 10\ \mathrm{g\ L^{-1}}$ rises to 5 days for an anhydrite (001) surface and is longer than one week in the cases of anhydrite (010) and (100) surfaces. The continuous celestite layer becomes progressively thicker as the interaction progresses and the celestite–anhydrite interface moves inwards within the anhydrite crystal. Thus, after 7 days interaction with a solution bearing Sr ($[\mathrm{Sr}]_{\mathrm{aq}} = 50\ \mathrm{g\ L^{-1}}$), the celestite layer parallel to the original anhydrite (001) substrate reaches 120 microns while the celestite layer parallel to the original anhydrite (010) substrate has a thickness of 40 microns (Fig. 4a). The precipitation of celestite in the bulk solution is not observed.

Overgrown celestite initially appears as micrometer-sized single crystals that grow oriented on the anhydrite surfaces studied (Fig. 4b and S4†). Celestite crystal habit is mainly defined by flat faces belonging to the {001} pinacoid and the {210} prism. Though less developed, some crystals also show faces that belong to the {101} prism (Fig. 3b). Some differences are observed between the habits of celestite crystals that grow on different anhydrite surfaces. Furthermore, celestite crystals undergo significant morphological changes during growth (Fig. S4†). Epitactic relationships between celestite and each anhydrite substrate

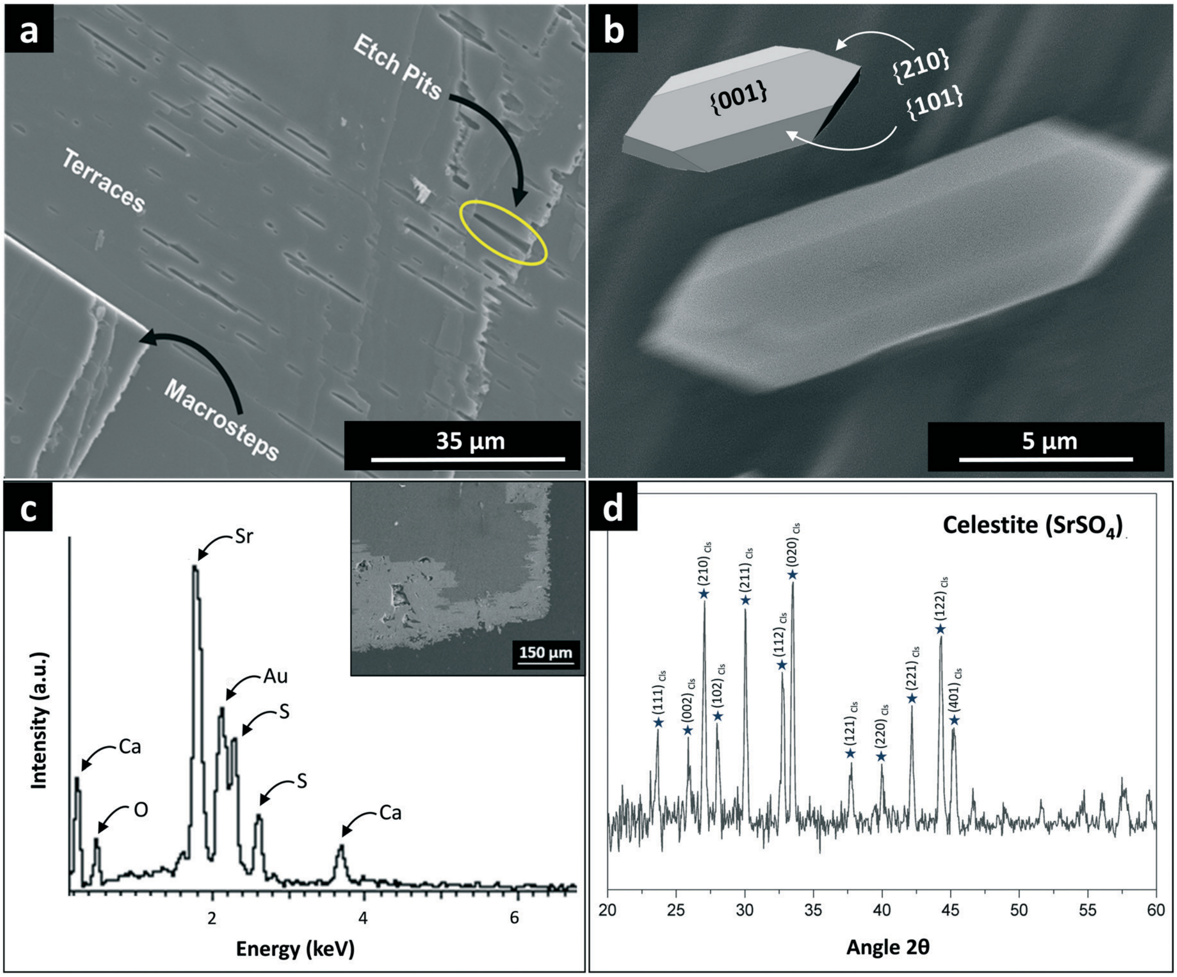

Fig. 3 (a) SEM image of an anhydrite (100) cleavage surface after 30 minutes interaction with pure water. Anhydrite surfaces are characterized by the presence of flat terraces and large macrosteps. Once the dissolution of anhydrite starts, etch pits develop on the terraces. The orientation and geometry of these pits allow us to identify main crystallographic directions on the substrate. (b) The interaction of the anhydrite surfaces with aqueous solutions bearing [Sr] ≥ 1 g L^{-1} leads to the formation of celestite single crystals, with a habit defined by a combination of the {001} pinacoid and the {210} and {101} rhombic prisms (see the drawing). The image shows a celestite crystal grown on an anhydrite (100) surface after 2 hours interaction with a Sr-bearing aqueous solution ($[Sr]_{aq}$ = 1 g L^{-1}). (c) A typical EDX analysis obtained in an epoxy-embedded cross-cut section of an anhydrite crystal interacted with a $[Sr]_{aq}$ = 50 g L^{-1} for 7 days showing that the newly formed crystals have a composition consistent with that of Ca-bearing celestite. (d) Glancing incidence X-ray diffraction pattern (0.1°) recorded after 2 hours of interaction between an anhydrite (001) surface and a $[Sr]_{aq}$ = 50 g L^{-1} aqueous solution. All diffraction peaks in the GIXRD pattern match well those of celestite, although some of them appear slightly shifted towards higher values of 2θ.

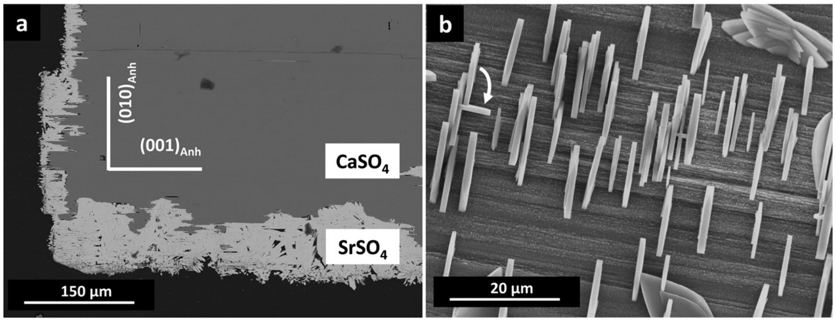

Fig. 4 (a) BSE image of an anhydrite crystal cross-cut along (100) after 7 days interaction with a Sr-bearing aqueous solution ($[Sr]_{aq}$ = 50 g L^{-1}). The different thickness of the replaced-by-celestite layer reflects the different reactivity of the $(001)_{Anh}$ and $(010)_{Anh}$ surfaces. (b) Celestite secondary crystals grown clearly oriented on an anhydrite (001) substrate that had interacted with a Sr-bearing aqueous solution ($[Sr]_{aq}$ = 1 g L^{-1}) during 1 hour.

as well as substrate-specific celestite morphological features and their evolution are described in the following sections.

Celestite overgrowth on anhydrite (100)

Crystallographic directions on anhydrite (100) surfaces are identified based on its dissolution features, which mainly consist in shallow, pencil-shaped etch-pits elongated along [001].[54] Celestite crystals that form on anhydrite (100) surfaces upon interaction with Sr-bearing aqueous solutions preferentially nucleate on edges of these etch pits or in nearby areas (Fig. S4a†). The habit of these crystals is defined by faces that belong to the {001} pinacoid and, to a lesser extent, to the {210} and {101} prisms.

Celestite secondary crystals grow oriented with respect to the anhydrite substrate with their {001} pinacoid parallel to the anhydrite (100) substrate (Fig. 5a). Two populations can be distinguished among these oriented celestite crystals. One population includes numerous individuals and consists of crystals that grow with their <120> edges parallel to anhydrite [010] direction (Fig. 5b; yellow star). The other population comprises fewer celestite crystals, and these are oriented with their <120> edges parallel to [001] direction in the anhydrite substrate (Fig. 5b; red star). The local coalescence of celestite crystals belonging to each of these populations leads to the formation of simple twins (Fig. 5b and c). Furthermore, the coalescence of celestite crystals of the same population but with different orientation due to existence of symmetry operators (mirror planes and 2-fold axis) inherent to the anhydrite structure and normal to the anhydrite (100) surface can also lead to the formation simple twins (Fig. 5b). As interaction between anhydrite (100) surface and Sr-bearing solutions progresses and celestite crystals continue to grow, they develop disoriented subunits, whose number increases along time and is accompanied by a progressive loss of parallelism between celestite and anhydrite directions. As can be seen in Fig. 5d and S4b,† the development of subunits in celestite crystals growing epitaxially on anhydrite (100) involves two combined misorientational spreads. One spread is associated to a progressive loss of parallelism between $(001)_{\mathrm{Clt}}$ and $(100)_{\mathrm{Anh}}$, while the other comprises a gradual loss of parallelism

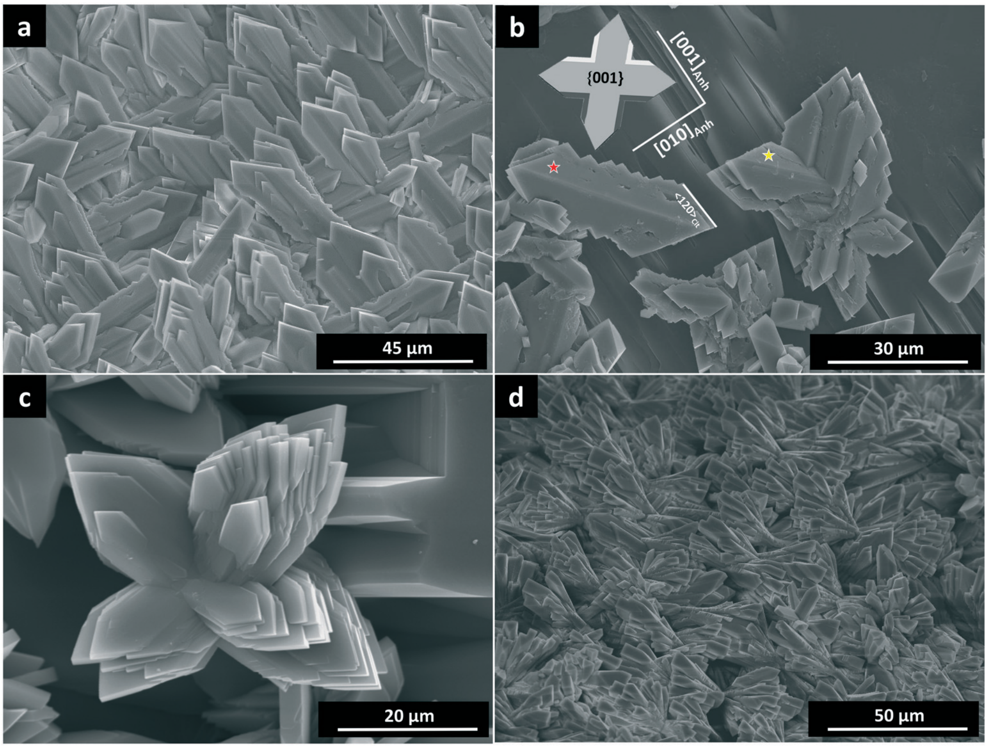

Fig. 5 SEM micrographs showing the formation of celestite crystals on anhydrite (100) surface after interacting with aqueous solutions bearing different Sr concentrations during different times. (a) A continuous layer consisting of densely packed oriented celestite crystals carpets the anhydrite substrate after 5 days interaction ($[\mathrm{Sr}]_{\mathrm{aq}}$ = 50 g L^{-1}). (b) The interaction of anhydrite (100) surfaces with both pure water and Sr-bearing aqueous solutions results in the early formation of etch pits that run parallel to [001]. When the interaction occurs with aqueous solutions with $[\mathrm{Sr}]_{\mathrm{aq}} \geq 1$ g L^{-1}, the epitactic nucleation of secondary celestite crystals is also observed. The epitaxy between anhydrite and celestite involves the matching of the plane (100) of anhydrite with the plane (001) of celestite. Celestite <120> edges are parallel to the [010] direction in the anhydrite substrate (yellow star) and, to a lesser extent, to the [001] direction in the anhydrite substrate (red star). The SEM micrograph shows the (100) surface of an anhydrite crystal after a 5 days interaction with an aqueous solution with $[\mathrm{Sr}]_{\mathrm{aq}}$ = 10 g L^{-1} (c) The coalescence of two neighbored celestite crystals with different epitactic orientations leads to the formation of simple twins ($[\mathrm{Sr}]_{\mathrm{aq}}$ = 10 g L^{-1}; interaction time 5 days). (d) Celestite crystals develop progressively misoriented subunits as their growth progresses. These misoriented units are apparent in celestite crystals formed on anhydrite (100) surface after 7 days interaction with an aqueous solution bearing 10 g L^{-1} Sr.

between $[120]_{Clt}$ and both $[010]_{Anh}$ and $[001]_{Anh}$. Maximum orientational spreads reach 20° after 5 days interaction.

Celestite overgrowth on anhydrite (001)

Etch pits formed on anhydrite (001) surface in contact with Sr-bearing aqueous solutions are elongated along [100] and bounded by steps parallel to [100] and [010].[54] The coalescence of these oriented etch pits results in the formation of evenly spaced grooves that run along [100]. These grooves are deep and give anhydrite (001) surface a very rough appearance. Celestite crystals nucleate on the edges of these grooves soon after the beginning of anhydrite interaction with the Sr-bearing aqueous solution. On anhydrite (001), celestite crystals show a rhombus-like habit, dominated by faces corresponding to the {001} pinacoid and the {210} prism (Fig. 4b, 6a and S4c†). These crystals grow with one face of their {210} prisms laying in direct contact with the anhydrite (001) substrate, $(001)_{Anh}\|(210)_{Clt}$, and their larger faces, those corresponding to the {001} pinacoid, oriented perpendicular to both, the anhydrite substrate and the deep grooves on it, so that $\{001\}_{Clt} \perp (001)_{Anh}$ and $[100]_{Anh}$ (Fig. 6). As a result, celestite [120] edges (defined by the intersection of {210} and {001} forms) appear oriented parallel to $[010]_{Anh}$, while [001] edges (defined by the intersection of faces corresponding to the {210} form) are oriented parallel to $[100]_{Anh}$ (Fig. 6b and c). Two approximately equally abundant orientations of celestite crystals can be distinguished (Fig. 6a). These two orientations are related by a mirror plane symmetry operator parallel to anhydrite [100] direction, this is, the direction of the grooves on the anhydrite (001) substrate (Fig. 6c). Additionally, another much less abundant population of celestite crystals oriented with their [120] edges parallel to $[100]_{Anh}$ is also observed (Fig. 4b; white arrow).

Similarly to the observed on anhydrite (100) substrate, epitactic celestite crystals that grow on an anhydrite (001) substrate progressively develop increasingly misoriented subunits and evolve from single crystals to crystal aggregates. This evolution is significantly more marked in the region of the celestite crystal that directly lays in contact with the anhydrite (001) substrate (Fig. 6a). In this region (marked with a red ellipse in Fig. 6b) subunits develop due to the combination of two different misorientational spreads. One spread involves the progressive loss of parallelism between $(001)_{Clt}$ and $[010]_{Anh}$ while the celestite plane remains perpendicular to $(001)_{Anh}$. The

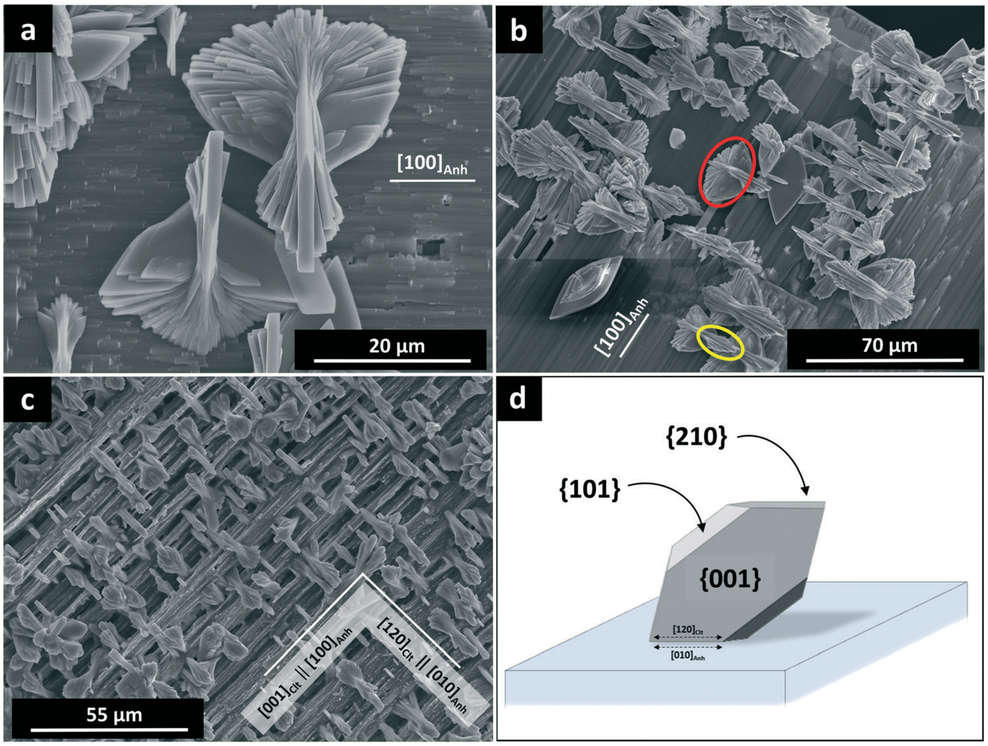

Fig. 6 SEM images showing celestite crystals that grow on anhydrite (001) surfaces. (a and b) Celestite crystals grow oriented so that $(001)_{Anh}\|(210)_{Clt}$. The epitaxy between both phases involves the matching of the plane (001) of anhydrite with the plane (210) of celestite. Celestite <120> edges run parallel to [010] direction in the anhydrite substrate. The existence of a mirror plane perpendicular to anhydrite (001) substrate generates two populations of celestite crystals. (c) Celestite single crystals progressively develop subunits during growth. These subunits are arranged according to two orientational spreads. Wider orientational spread occurs in the region of the celestite crystal that is closer to the substrate, which leads to the development of a swan-like habit. (d). Simulation of a typical celestite crystal growing on an anhydrite (001) cleavage surface. ((a): $[Sr]_{aq}$ = 10 g L^{-1} (a), interaction time = 2 hours; (b) $[Sr]_{aq}$ = 1 g L^{-1}, interaction time = 2 hours; (c) $[Sr]_{aq}$ = 10 g L^{-1}, interaction time = 2 hours).

other spread arises from the progressive tilting in the orientation of $(001)_{Clt}$, which evolves from perpendicular to parallel to $(001)_{Anh}$. The combination of both misorientational spreads gives a swan like-shape to these crystals, where the misorientational spread between subunits can reach up to 180° (Fig. 6a). In contrast, orientational spread in the region of the celestite crystal that does not directly lays in contact with the anhydrite (001) substrate (marked with a yellow ellipse in Fig. 6b) exclusively arises from the change in the orientation of $(001)_{Clt}$, which despite progressively losing its parallelism to $[010]_{Anh}$ remains perpendicular to $(001)_{Anh}$. In this case, the maximum misorientation between crystal subunits only reaches up to 45°. The peculiar swan like morphology of celestite crystal aggregates resulting from the development of the described misorientational spreads is depicted in Fig. 6, where a simulation of a typical celestite crystal growing on anhydrite (001) surface as a result of the interaction of the later with a Sr-bearing aqueous solution has been included (Fig. 6d).

Celestite overgrowth on anhydrite (010)

Etch pits formed on anhydrite (010) surface upon dissolution in contact with Sr-bearing aqueous solutions are shallow and rectangular-shaped (Fig. 7). These pits appear elongated along [001] and bounded by steps parallel to [100] and [001].[54] A small population of platy and rhombus-shaped celestite crystals whose habit is dominated by the {001} pinacoid also forms on anhydrite (010) substrates. All these crystals grow on either cleavage macrosteps or steps bounding etch pits. Both the absence of celestite crystals growing on terraces and the much smaller celestite crystal density on this substrate compared to that observed on anhydrite (100) and (001) surfaces points to celestite nucleation actually taking place on the two latter surfaces, where these two planes are exposed on steps, rather than directly on anhydrite (010). SEM observations suggest that celestite crystals that grow on anhydrite (010) substrates also develop a certain degree of misorientational spread that leads to the formation of subunits (Fig. S4f†). However, the characteristics of this misorientational spread are much more difficult to evaluate due to the smaller number and size of celestite crystals that grow on this anhydrite substrate together to their unclear epitactic relationships with respect to the anhydrite (010) substrate.

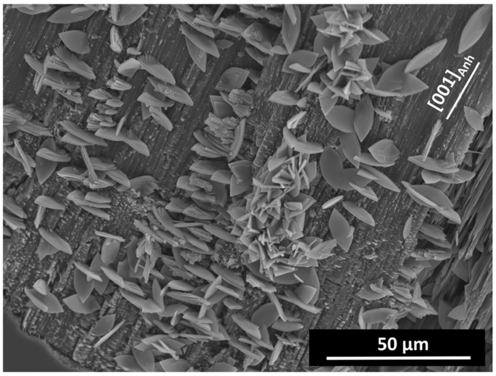

Fig. 7 SEM micrograph of an anhydrite (010) surface after interaction with Sr-bearing aqueous solutions ($[Sr]_{aq}$ = 1 g L^{-1}; interaction time = 2 hours). The interaction promotes the formation of celestite crystals poorly oriented with respect to the anhydrite substrate.

Texture analysis

The Rietveld processing results in a good data fit (Fig. 8), which ensures a convergence of the refined parameters. The refinement of celestite cell parameters shows a shortening reduction of all of them compared to their lengths in the reference structure,[41] with their mean values for the three anhydrite substrate orientation being a = 8.380, b = 5.324 and c = 6.876.

Recalculated celestite 001, 100, 110, 101, 210 and 120 pole figures for each anhydrite orientation ($(100)_{Anh}$, $(001)_{Anh}$ and $(010)_{Anh}$) are shown in Fig. 9.

In all the samples, celestite preferred orientation with different geometrical relationships to the anhydrite substrate is observed. Celestite overgrowths on $(100)_{Anh}$ show the strongest texture, with most of the celestite crystals showing preferred orientation (pole figure minimum = 0.1 m.r.d. Fig. 9a). In contrast, on $(001)_{Anh}$ and $(010)_{Anh}$, although most crystals are preferentially oriented, there is a significant proportion of them that appear randomly oriented, with minima ranging from 0.48 to 0.39 m.r.d (Fig. 9c to f).

Overall, most of celestite crystals fit into two textural components (A and B; Fig. 9), which can directly be correlated with the overgrowth patterns that can be observed in SEM micrographs corresponding to Fig. 5 and 6.

Celestite texture on anhydrite (100)

Celestite texture on anhydrite (100) has the strongest preferred orientation, with an F^2 = 6.1087 and a pole figure max/min = 3.97/0.1 m.r.d. (Fig. 9a). Two textural components are identified. Component A is defined by celestite crystals with their (001) poles distributed in two maxima around anhydrite [100] (//Z axis) and elongated preferably along the X-axis (//$[010]_{Anh}$). The angular dispersion around the Z-axis is about 50°. Furthermore, celestite (210) poles show two peripheral maxima parallel to the X- and Y-axes, separated 70–80°. A similar pattern is observed for $(120)_{Clt}$ poles.

In the textural component B, celestite (001) poles show an elongated maximum parallel to the Y-axis, with an angular dispersion of 35° in the YZ plane and 25° in the XY plane. Celestite (210) poles define a small maximum and an incomplete girdle between X and Y axes at 30° and 50–60°, respectively, from Z-axis.

Celestite texture on anhydrite (001)

Texture strength of celestite on this plane is F^2 = 2.3363, and pole figure max./min. = 1.92/0.48 m.r.d (Fig. 9c). Overall, there is a significant number of celestite crystals randomly oriented (0.48 m.r.d.). Textural component A includes numerous celestite crystals with their (210) poles parallel to $[001]_{Anh}$ (//Z axis) and an angular dispersion (*ca.* 15°) about anhydrite [001]. A second

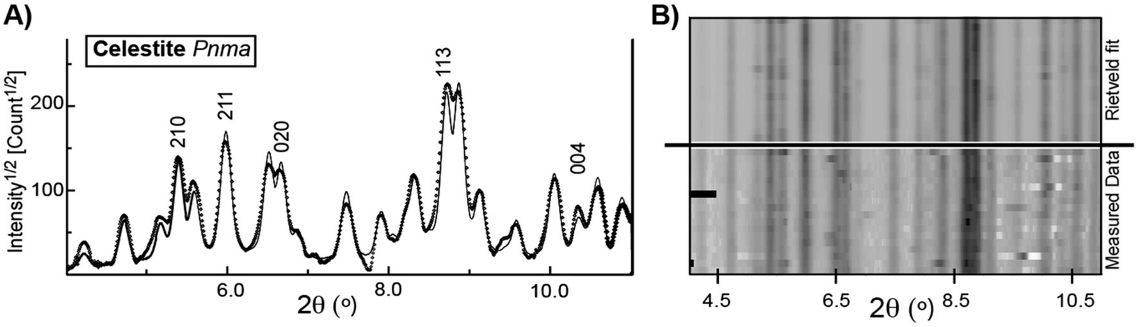

Fig. 8 A) Total profile obtained by integrating 216 spectra from 0° to 360° azimuth. Experimental data are shown as dots and the line is the Rietveld fit. Some planes are indexed. B) 'Unrolled' diffraction image showing intensity variations due to texture. The Rietveld fit on top reproduce well the measured diffraction data below.

(210) point maximum is identified in the *X*-axis at 76°. The $(120)_{Clt}$ and $(100)_{Clt}$ poles are also concentrated in the surroundings of the *Z*-axis (//$[001]_{Anh}$) (±20°). The peripheral distribution of the $(001)_{Clt}$ poles around $[100]_{Anh}$ (±30°) is consistent with textural component A.

Celestite crystals in component B depict a stronger texture, with $(001)_{Clt}//(001)_{Anh}$ (±20–30°, maximum dispersion 56° along *X* and *Y*-axes). A set of $(210)_{Clt}$ poles concentrate between 16 and 30° from $[100]_{Anh}$ along the *Y*-axis. A projection of $(210)_{Clt}$ along *X*-axis is geometrically consistent and partially overlaps with A-component, what prevents a detailed distinction. Moreover, $(100)_{Clt}$ peripheral girdle and a point maximum close to $[100]_{Anh}$ (±20°) are a coherent part of the B-component.

Celestite texture on anhydrite (010)

SEM observations showed no oriented celestite overgrowths on $(010)_{Anh}$ (Fig. 7). Texture analysis, however, shows distinct pole patterns (Fig. 9e and f) and a considerable strength (F^2 = 6.1055), with pole figure maximum and minimum of 2.77 and 0.39 m.r.d. Most celestite crystals have their (001) poles parallel to the *X* axis (//$[001]_{Anh}$) with an angular dispersion of ±75° in the *XY* plane, and ±30°in the *XZ* plane of the reference system (Fig. 1). The $(001)_{Clt}$ poles depict two secondary point maxima, which fall along *Y*-axis, representing $(001)_{Clt}$ planes at ±50° to the $(010)_{Anh}$ substrate. $(210)_{Clt}$ poles show a peripheral distribution close to the *X*-axis and between *X*- and *Y*-axes. Other point maxima of $(210)_{Clt}$ poles fall close to the *Y*-axis, forming an angle of 40° and 60° with the substrate. Geometrical constraints suggest that celestite texture is compatible with a mixture of two populations developed on step and pit edges, where $(100)_{Anh}$ and $(001)_{Anh}$ surfaces are exposed (inset; Fig. 9e).

Discussion

We observe that the interaction of any of the three main anhydrite cleavage surfaces with aqueous solutions bearing $[Sr]_{aq} \geq 1$ g L^{-1} leads to the precipitation of celestite crystals that grow oriented with respect to the anhydrite substrate. When the interaction starts, the Sr-bearing solution contains no sulfate and its supersaturation with respect to both anhydrite and celestite is zero. The dissolution of the anhydrite substrate results in the release of SO_4^{2-} and Ca^{2+} ions to the aqueous solutions, whose supersaturation with respect to celestite rapidly increases to overcome a threshold supersaturation for celestite heterogeneous nucleation before the aqueous solution becomes saturated with respect to anhydrite in the case of those solution with initial $[Sr]_{aq} \geq 1$ g L^{-1}. The concept of threshold supersaturation is equivalent to that of critical supersaturation but applies to systems where supersaturation evolves along time. The threshold supersaturation value is not unique but depends on the rate at which the systems moves from equilibrium, this is the supersaturation rate.[55–57] Thus, it will be higher the faster the substrate dissolves and SO_4^{2-} and Ca^{2+} ions are released to the aqueous solution. The nucleation and growth of celestite crystals removes SO_4^{2-} ions, as well as Sr^{2+}, from the solution and promotes further dissolution of the anhydrite substrate, which in turn results in the solution again becoming supersaturated with respect to celestite, thereby facilitating the growth of celestite crystals. In this way, a dissolution–crystallization feedback loop is stablished, which operates as long as the system does not become exhausted of either anhydrite and/or dissolved Sr or the celestite does not completely armor the anhydrite substrate from interaction with the solution. This loop operates according to the following reactions:

$$CaSO_{4(s)} + nH_2O_{(l)} \rightarrow Ca^{2+}{}_{(aq)} + SO_4{}^{2-}{}_{(aq)} + nH_2O_{(l)} \quad (1)$$

$$SO_4{}^{2-}{}_{(aq)} + Sr^{2+}{}_{(aq)} \rightarrow SrSO_{4(s)}\downarrow\downarrow \quad (2)$$

As stated above, we observe the formation of a significantly higher density of celestite crystals on $(001)_{Anh}$ than on $(100)_{Anh}$ and $(010)_{Anh}$. This higher crystal density can be explained if we take into account the dissolution kinetics of the three anhydrite substrates. *In situ* atomic force microscopy experiments conducted by Shindo *et al.*[54] evidenced that the dissolution of $(001)_{Anh}$ in contact with water takes place at a much faster rate than the dissolution of $(100)_{Anh}$ and $(010)_{Anh}$. It stands to reason that $(001)_{Anh}$ will also dissolve at a much faster rate than

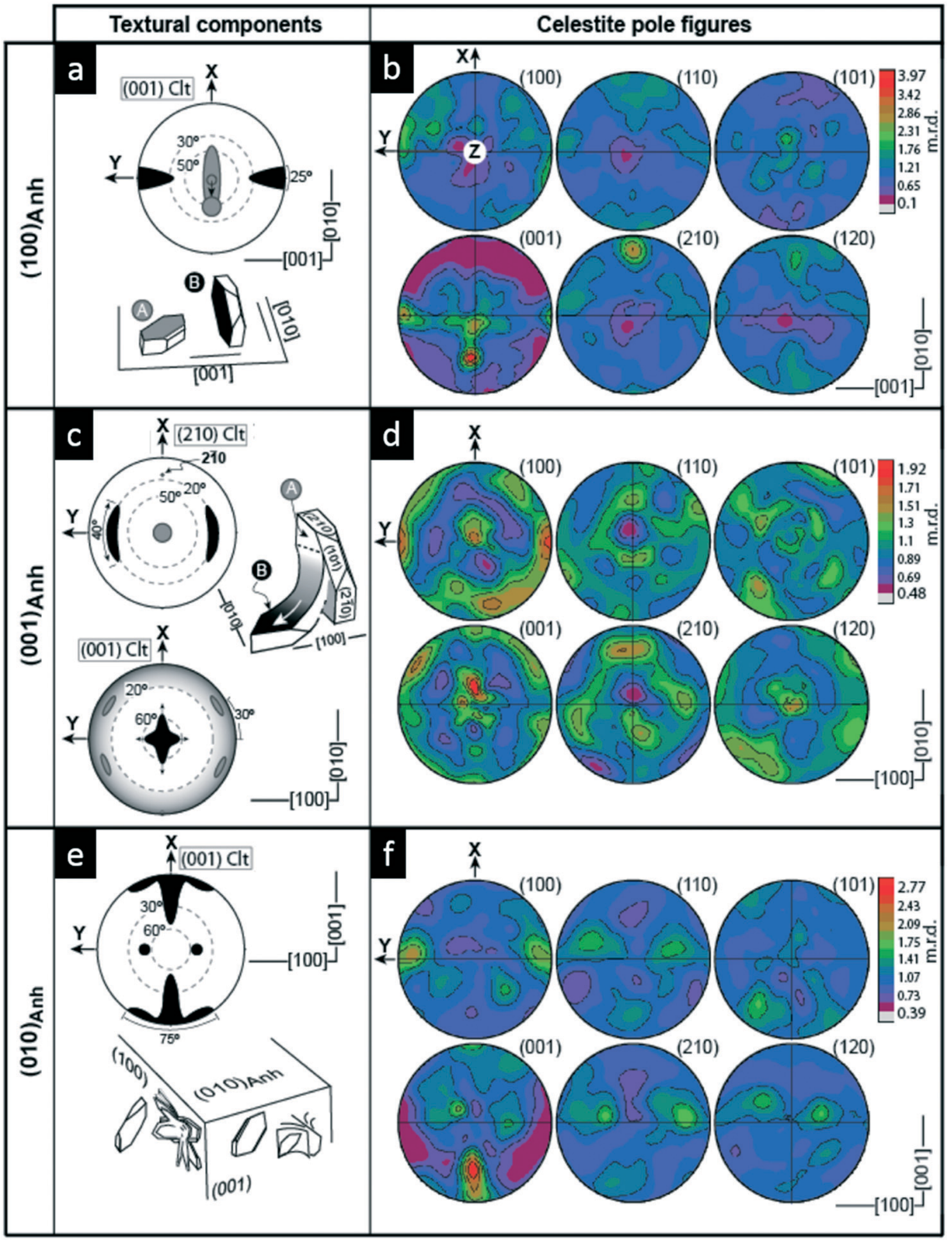

Fig. 9 Pole figures of celestite crystals growing on the three anhydrite substrates considered: a and b) $(100)_{Anh}$, c and d) $(001)_{Anh}$ and e and f) $(010)_{Anh}$. On the left column, main textural components: $(001)_{Clt}$ and $(210)_{Clt}$ (A: grey; B: black) are summarized in stereographic projection. Dashed circles represent different angles to the anhydrite substrate. Main epitactic relationships are illustrated with simple schemes on each case (see Fig. 10 and 11). The absence of oriented celestite overgrowth on $(010)_{Anh}$ suggests that texture in this surface arises from mixing crystals growing on $(100)_{Anh}$ and $(001)_{Anh}$ steps and/or edge pits exposed in this surface (Fig. 7). The reference system *XYZ* has been defined in Fig. 1 and indicates the orientation of anhydrite directions ([100], [010] and [001]) for each plane. Equal angle projections are marked with linear contour intervals (m.r.d.: multiples of a random distribution).

$(100)_{Anh}$ and $(010)_{Anh}$ in contact with a Sr-bearing aqueous solution, which will result in a Sr-bearing solution in contact with $(001)_{Anh}$ becoming supersaturated with respect to celestite at a faster rate than a solution in contact with the two latter surfaces. Assuming that anhydrite dissolution is the rate limiting step in the dissolution–crystallization reaction, the faster dissolution of $(001)_{Anh}$ will result in the dissolution–crystallization loop also operating at a faster rate when the Sr-bearing solution interacts with this substrate.

Regardless of the anhydrite surface considered, celestite crystals show habits dominated by the {001} pinacoid, combined with the {210} and {101} prisms, which appear less developed. All these forms are common in natural celestite crystals.[58] Moreover, they define the theoretical habit of celestite, according to the periodic bond chain (PBC) analysis conducted by Hartman and Strom[59] for crystals with the barite structure. This analysis attributes the lowest attachment energy to the {001} form, which explains that it is the most developed form in all the newly formed celestite crystals, regardless of the anhydrite substrate on which they are growing.

Epitactic relationships between anhydrite and celestite

The structural matching between the overgrowth and the substrate is a key parameter that must be considered in order to understand the development of an epitaxy. A good matching between layers of two different phases requires that their structures share both, geometrical features and structural elements. Despite crystallizing in different systems, anhydrite (space group *Amma*, a = 6.993 Å, b = 6.995 Å, and c = 6.245 Å)[42] and celestite (space group *Pnma*, a = 8.360 Å, b = 5.352 Å, c = 6.858 Å),[41] it does exist a clear affinity between the structures of these phases. Indeed, both structures are orthorhombic and consist of sulfate – cation chains linked into sheets which in turn are linked together to build up a framework. As a result, the formation of (001) and (210) layers of celestite onto the (100) and (001) surfaces of anhydrite does not result in the interruption of the sulfate – cation sequences but guarantees their continuity, thereby also ensuring the structural continuity between the two phases involved in the epitaxy. This structural continuity through the interphase constitutes a basic requirement condition for the existence of epitactic relationships between two crystalline individuals.[60] On the other hand, in all the epitactic relationships described above between the celestite and the three anhydrite substrates considered, the matching between the structure of these two phases involves crystallographic directions that are parallel to PBCs: in the structure of anhydrite, three PBCs run parallel to its main crystallographic axes, whereas in the structure of celestite the most stable PBCs run parallel to [001] and <120>. According to the PBC theory,[17] this scenario favors the development of an epitaxy since a minimum interface energy is achieved when there is a coincidence between close-packed atomic rows (defined by the PBCs).

Beyond structural considerations, the formation of an epitaxy also requires low misfit values between the lattice planes involved. Lattice misfit (mf) can be expressed by means of the equation (van der Merwe, 1978):[19]

$$\mathrm{mf}(\%) = \frac{t_{[uvw]\mathrm{Cls}} - t_{[uvw]\mathrm{Anh}}}{t_{[uvw]\mathrm{Anh}}} \times 100 \qquad (3)$$

where $t_{[uvw]}$ is the repeating period (distance between successive equivalent SO_4 groups) along the [*uvw*] direction of the substrate (anhydrite) and overgrowth (celestite). Negative misfit values mean that the unit cell of the overgrowth is contracted along [*uvw*] in comparison to the unit cell of the substrate ($t_{[uvw]\mathrm{Clt}} < t_{[uvw]\mathrm{Anh}}$). Similar repeating periods (mf ≤ |10|% to |12|%) mean a good matching between the two structures and favour the formation of an epitaxy.[11,19,23] Table 1 shows the misfits calculated for the shared directions between celestite and anhydrite defined in the epitaxy. In all the cases, mf ≤ |10|%, which puts them within the acceptable limits for the formation of an orientated overgrowth of celestite on the substrate of anhydrite. The matching between the two structures through the $(001)_{\mathrm{Anh}}$ and $(210)_{\mathrm{Clt}}$ is remarkably good, with linear misfits that are lower than |3|% for all the shared directions involved in the epitaxy. Moreover, the fact that a and b axes in anhydrite are almost identical in length (b–a = 0.002 Å) explains the existence of two different populations of celestite, whose orientations are related by a pseudo 4-fold axis. Additionally, the less good matching between $[001]_{\mathrm{Anh}}$ and $[120]_{\mathrm{Clt}}$ (8.74%) through anhydrite (100) surfaces explains that the population of celestite crystals that show this orientation is much less numerous than the one formed by celestite crystals oriented so that $[120]_{\mathrm{Clt}}$ and $[010]_{\mathrm{Anh}}$ are parallel, since a much better matching (−2.91%) exists between these two latter directions through anhydrite (100) surfaces (Fig. 5b).

As has been explained, on all the anhydrite surfaces studied several populations of differently orientated celestite crystals are observed. For a given anhydrite substrate the orientations shown by the celestite crystals that grow on it are related by symmetry operators which belong to the symmetry class of anhydrite (2/*m* 2/*m* 2/*m*) and are perpendicular to that substrate. The coalescence of differently oriented individuals as a result of their growth leads to the formation of twins. "Substrate induced twinning" is a well-documented phenomenon which can lead to the generation of specific textures.[61,62] The occurrence of substrate induced twinning has already been reported associated to numerous dissolution–crystallization reactions that involve sulfate, carbonate and/or phosphate mineral phases.[16,23,62] One of these dissolution–crystallization reactions involves the interaction of Pb-bearing aqueous solutions with anhydrite, which leads to the precipitation of anglesite ($PbSO_4$) on anhydrite surfaces.[23] Both, anglesite and

Table 1 Epitactic relationships between anhydrite and celestite

Anhydrite ($CaSO_4$)		Celestite ($SrSO_4$)			Misfit (%)
Contact plane	Parameter (Å)	Contact plane	Parameter (Å)	Population	
(100)	2 × [010] = 13.990 Å	(001)	[120] = 13.582 Å	1	−2.91
	2 × [001] = 12.490 Å			2	8.74
(001)	2 × [010] = 13.990 Å	(210)	[120] = 13.582 Å	3	−2.91
	[100] = 6.993 Å		[001] = 6.858 Å		1.93
	2 × [100] = 13.986 Å		[120] = 13.582 Å	4	−2.88
	[010] = 6.995 Å		[001] = 6.858 Å		−1.96

celestite belong to the barite group and, consequently, are isostructural. As reported by Morales *et al.*,[23] anglesite crystals also grow oriented on $(100)_{Anh}$, $(010)_{Anh}$ and $(001)_{Anh}$, showing identical epitactic relationships with these substrates as described here for celestite.

The most striking difference between celestite and anglesite crystals growing on $(100)_{Anh}$, $(010)_{Anh}$ and $(001)_{Anh}$ regards the evolution of the characteristics of anglesite and celestite crystals during growth. While anglesite crystals show no sign of branching and split growth and, consequently, their orientation with respect to a given anhydrite substrate remains the same as they grow, celestite crystals progressively develop subunits as their growth progresses, concomitantly losing their single crystal character and their epitactic orientation with respect to the anhydrite substrate. We interpret the marked splitting that results in the evolution of celestite crystals from single to crystal aggregates as probably driven by the incorporation of small amounts of Ca into the structure of celestite substituting Sr. While no Ca incorporation was detected in the case of anglesite, most likely due to the very large difference between the radii of Pb^{XII} (1.49 Å) and Ca^{XII} (1.34 Å), celestite growing on anhydrite has up to 1.5 wt% Ca, as determined by EDX analysis. Still, the ionic radii of Sr^{XII} (1.44 Å) and Ca also are significantly different and Ca incorporation in Sr positions is due to stress celestite structure. The formation of dislocations is a common way for crystal structures to release lattice strain.[63] These dislocations can appear spatially arranged at regular intervals, leading to the formation of small-angle boundaries.[30,60,63] Between dislocations the lattice will be coherently continuous across these boundaries. This impurity incorporation-related splitting mechanisms explains, for example, the formation of sheaf-like and spherulitic morphologies in Mg-calcites.[64,65] Small-angle boundaries define individual subunits in celestite aggregates. Besides, the reduction of epitactic celestite cell parameters (*ca.* 1.3%) supports the Sr–Ca substitution model. Thus, we conclude that the incorporation of Ca in the celestite growth steps causes the formation of small-angle boundary and leads to the marked splitting of the celestite crystals involved in the development of sheaf-like aggregates (Fig. 5b) on the $(100)_{Anh}$ surface and swan-like aggregates on the $(001)_{Anh}$ surface (Fig. 6). The anisotropic features of the splitting that leads to the formation of the latter aggregates may be related to the development of sharp Ca^{2+} and SO_4^{2-} concentration gradients at the anhydrite–aqueous solution interface (boundary layer) as soon as the anhydrite substrate starts to dissolve. The development of such compositional gradients at the mineral–aqueous solution interface during dissolution–crystallization reactions has been experimentally confirmed in numerous systems.[66–69] These compositional gradients necessarily result in supersaturation gradients. Since coupled dissolution–precipitation reactions are kinetically faster than diffusion through the bulk aqueous solution, the region of the celestite crystals that directly lays in contact with the anhydrite (001) substrate grows under higher supersaturation conditions than regions further away from the substrate. This higher supersaturation would facilitate the incorporation of higher amounts of Ca, which in turn would explain the further development of misorientational spreads in the region of the celestite crystals in direct contact with the anhydrite (001) substrate.

As shown in cross-cut crystals (Fig. 4a and S2†), the replacement reaction of anhydrite by celestite seems to efficiently progress towards the core of the anhydrite crystals. For the replacement process to proceed, a continuous communication between the interface where the reaction occurs and the bulk solution is required.[40,67,69] This communication takes place through the formation of an intrinsic intergranular microporosity which guarantees a permanent supply of Sr^{2+} ions towards the calcium sulfate surface and those can react with the SO_4^{2-} released to the fluid as a result of mineral dissolution. As stated in the introduction, the formation of an epitaxy can be a major drawback for the development of dissolution crystallization reactions because its formation can, in certain cases, efficiently passivate the surface of the primary mineral.[11–13] This frequently occurs when isostructural phases which belong to the same mineral group grow through the Frank van der Merwe epitactic growth mechanism.[18] Contrarily, when epitaxial growth involves greater misfit values, 3D nuclei of the secondary phase form on the primary one through the Volmer Weber or Stranski Krastanov epitactic growth mechanism.[14–17,23] Here, even if the overgrowth completely carpets the substrate of the primary mineral (like in the case of our celestite crystals growing on the anhydrite surfaces), the armoring is usually imperfect.[16,23] The anhydrite – celestite epitaxy described in this work clearly falls within the latter category. The coalescence of differently oriented celestite crystals on the anhydrite cleavage surfaces does not completely seal the substrate and allow the Sr-rich solution to penetrate towards the primary anhydrite surface. Hence, the anhydrite to celestite transformation can proceed. Additionally, we must take into consideration the characteristic morphological evolution of the epitaxial celestite overgrowth with elapsing interaction time. The development and coalescence of rough sheaf-like and swan-like aggregates will further diminish the armoring of the anhydrite substrate leading to the formation of extremely porous surfaces which will certainly facilitate even more the circulation of the aqueous solution through the replacing layer.

Celestite texture and epitactic growth on anhydrite

Quantitative texture analysis have shown distinct textural components of celestite crystals growing on anhydrite faces. $(001)_{Clt}$ and $(210)_{Clt}$ pole figures are particularly relevant to correlate texture and morphological features as observed under SEM. Two main textural components (A and B, Fig. 9) are clearly observed in $(100)_{Anh}$ and $(001)_{Anh}$ substrates. In contrast, celestite texture on $(010)_{Anh}$ shows a more complex pattern, which we interpret as arising from the mixed contribution of celestite crystals that nucleate oriented on steps and edge pits. On these edges, $(100)_{\rm Anh}$ and $(001)_{\rm Anh}$ surfaces are exposed to the interaction with the Sr-bearing aqueous solution. Thus, celestite texture on $(010)_{\rm Anh}$ would be the result of celestite epitactic growth on $(100)_{\rm Anh}$ and $(001)_{\rm Anh}$ rather than on the former surface. An explanative schematic of these orientational relationships is depicted in the left column of Fig. 9.

Celestite texture strength (F^2-index) differs on each anhydrite face: $(100)_{\rm Anh} > (001)_{\rm Anh} > (010)_{\rm Anh}$, and pole figure density in $(100)_{\rm Anh}$ is about two times higher than in $(001)_{\rm Anh}$ face. Interestingly most of celestite crystals on $(100)_{\rm Anh}$ are textured (pole figure minimum = 0.1 m.r.d.; Fig. 9), while a considerable number of celestite crystals on $(001)_{\rm Anh}$ are randomly distributed (minimum = 0.48 m.r.d.).

Simple geometrical models have been elaborated to correlate celestite textural components and direct observation under the scanning electron microscope of celestite crystals grown on $(100)_{\rm Anh}$ (Fig. 10) and $(001)_{\rm Anh}$ (Fig. 11), respectively. In all cases pole figure orientation data are evaluated within the coordinate system defined in Fig. 1. As an example of the procedure, a detailed stereographic projection of a $(001)_{\rm Clt}$ plane inclined 60° to the substrate (*i.e.* $(100)_{\rm Anh}$) in the *XYZ* coordinate system is showed in Fig. 10a. The location of the pole (*P*) is equivalent to the one indicated in the real pole figure (Fig. 10b). $(001)_{\rm Clt}$ pole figure distribution depicts a quasi-orthorhombic symmetry in which two rotations of ±50° and ±30° are identified in the *X*- and *Y*-axis respectively (Fig. 10b). Textural component A (Fig. 9a) is compatible with a rotation of ±50° around the *Y*-axis $(//[001]_{\rm Anh})$ of celestite crystals initially oriented with $(001)_{\rm Clt}//(100)_{\rm Anh}$ and $<120>_{\rm Clt}//[001]_{\rm Anh}$ and $[010]_{\rm Anh}$ (Fig. 10c). Note that only one pair of twinned celestite crystals is represented in Fig. 10c for clarity, but substrate-induced twins have 4-folds symmetry (Fig. 5b, c and 10b). Crystal density is asymmetric along the *X*-axis, suggesting that one twinned pair is much more abundant than the other (Fig. 10b). This result is in good agreement with our SEM observations and the epitaxy model proposed. The component B could be conceived starting with celestite crystals originally oriented with $(001)_{\rm Clt}$//*Y*-axis and $(210)_{\rm Clt}$//*Z*-axis (Fig. 10d), then followed by a rotation of ±30° around the *X*-axis $(//[001]_{\rm Anh})$ (Fig. 10b and d). This model is compatible with the orientation distribution of the subunits constituting microscopic celestite aggregates (Fig. 5d).

Textural patterns of celestite overgrowths on $(001)_{\rm Anh}$ are compatible with the progressive development of disoriented celestite subunits (Fig. 11a). Textural component A represents

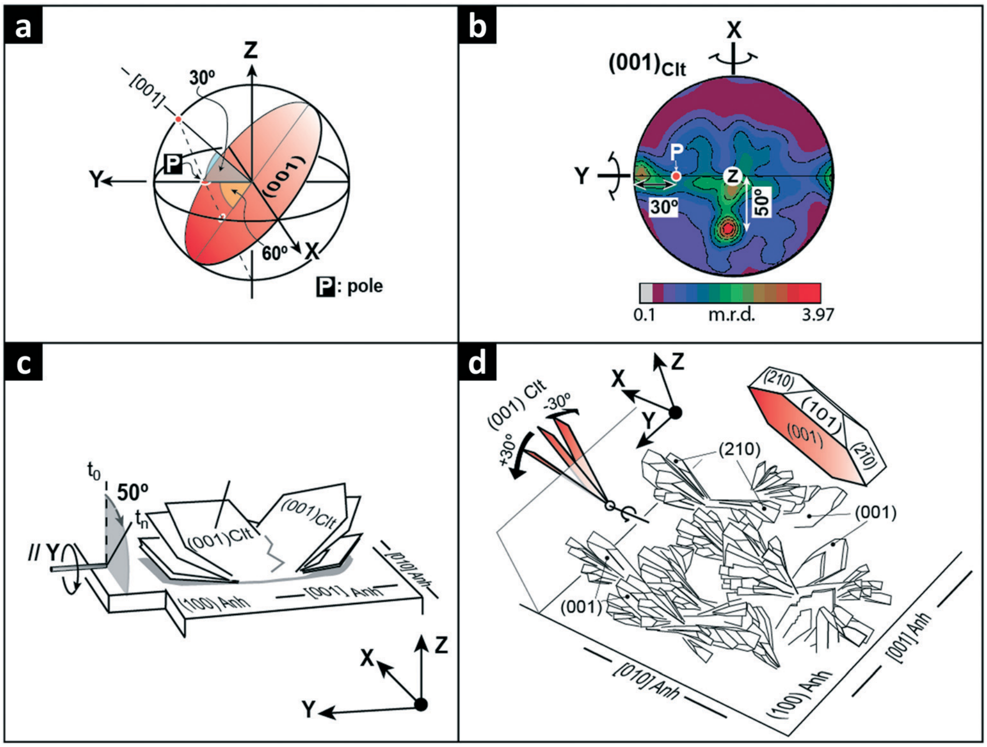

Fig. 10 Conceptual models for celestite textural components developed on $(100)_{\rm Anh}$ face (Fig. 9). a) 3D Upper hemisphere stereographic projection of a $(001)_{\rm Clt}$ plane inclined 60° to the substrate (*i.e.* $(100)_{\rm Anh}$) in the *XYZ* coordinate system. The plane is rotated around the *X*-axis. Note $(001)_{\rm Clt}$ pole (*P*) is the same in (b). b) Annotated $(001)_{\rm Clt}$ pole figure showing angular dispersion of poles along *X* and *Y*-axes which correspond to textural components A and B, respectively. Along the *X*-axis density distribution is asymmetric with respect to *YZ* plane, suggesting a lesser development of crystals along-*X* axis. c) Development of textural component A on $(100)_{\rm Anh}$ where progressive angular spreading occurs from $(001)_{\rm Clt}$ parallel to $(100)_{\rm Anh}$ (t_0) to ±50° around *Y*-axis (*i.e.* $//[001]_{\rm Anh}$; t_n). Only a pair of twinned crystals is represented for clarity, but a mirror pairs exist (see Fig. 5b). d) Celestite textural component B is the result of a rotation of crystals oriented with $(001)_{\rm Clt}//(001)_{\rm Anh}$ and $(210)_{\rm Clt}//(100)_{\rm Anh}$ (indexed large crystal) up to ±30°around the *X*-axis (see Fig. 5b).

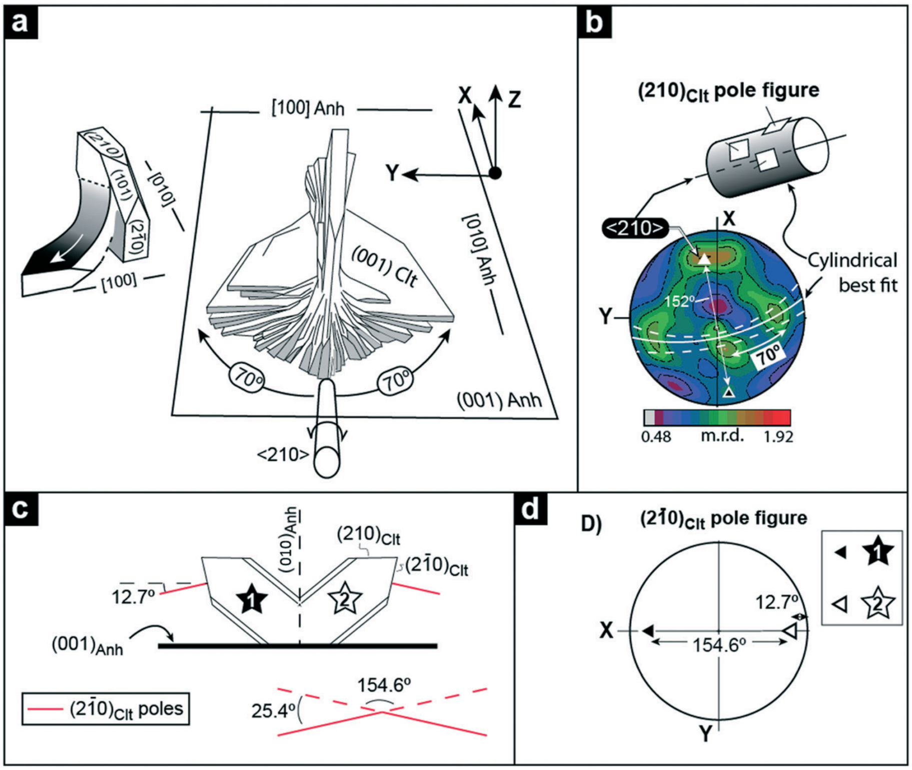

Fig. 11 Model for celestite textural components developed on $(001)_{\text{Anh}}$. a) Development of celestite subunits by an accumulated rotation (±70°) of crystals primary oriented with $(001)_{\text{Clt}}//(100)_{\text{Anh}}$ and $(210)_{\text{Clt}}//(001)_{\text{Anh}}$ (*i.e.* component A) around an $<hk0>_{\text{Clt}}$ (*e.g.* <210>), *ca.* *X*-axis. As a result, swan-like habit aggregates are generated (see Fig. 6). b) $(210)_{\text{Clt}}$ pole figure where cylindrical (white line) and conical (white dashed line) best fit has been calculated for $(210)_{\text{Clt}}$ point maxima. Symmetry rotational axis in both cases falls around $<210>_{\text{Clt}}$ maximum (white triangle). A conceptual sketch for a cylindrical best fit is included. Black triangle represents submaxima separated by 152° of white triangle and correlate with $(2–10)_{\text{Clt}}$ poles as explained in c) and d). c) Geometrical model of two celestite crystals (starts 1 and 2) whose growth on $(001)_{\text{Anh}}$ results in the formation of a substrate induced twin. The angular relationship between (2–10) poles (in red) of these crystals (154.6°) is depicted. Note that these crystals are related by a mirror plane parallel to $(010)_{\text{Anh}}$. d) Simplified $(210)_{\text{Clt}}$ pole figure showing the projection of (2–10) directions from crystal 1 (black triangle) and crystal 2 (white triangle). The twin plane will be parallel to *YZ* coordinate plane. Note the correlation with the real texture represented in b).

celestite crystals oriented with $(001)_{\text{Clt}}//(100)_{\text{Anh}}$ and $(210)_{\text{Clt}}//(001)_{\text{Anh}}$. An accumulated rotation of ±70° around $<hk0>_{\text{Clt}}$ (*e.g.* <210>), aligned to the *X*-axis, results into the textural component B (Fig. 11a and b) and the swan-like habit (Fig. 6). In the $(210)_{\text{Clt}}$ pole figure (Fig. 11b) conical and cylindrical best fit is calculated for main point maxima, which is indicative of a symmetry axis located around <210>.[70] The schematic drawing in Fig. 11c describes the substrate induced twinning of celestite crystals as interpreted from both, texture results and SEM observations on $(001)_{\text{Anh}}$. In the $(210)_{\text{Clt}}$ pole figure (Fig. 11b), two maxima are projected near the *X*-axis (white and black triangles). These maxima most likely correspond to the $(2–10)_{\text{Clt}}$ faces of the two populations of differently oriented swan-like aggregates related through a mirror plane parallel to $(010)_{\text{Anh}}$ and whose coalesce leads to the formation of substrate induced twins form, as depicted in Fig. 6. A scheme of this type of twins, consistent with the textural components derived from $(210)_{\text{Clt}}$ pole figure, is show in Fig. 11c. In this geometrical model two differently oriented celestite crystals (stars 1 and 2), both with (210) parallel to $(001)_{\text{Anh}}$, form a twin, with $(010)_{\text{Anh}}$ acting as the twin plane (parallel to *Y*-axis in Fig. 11d). The simplified $(210)_{\text{Clt}}$ pole figure in Fig. 11d shows the angular relationship between relevant (2–10) poles of crystals 1 and 2 (154.6°). This is consistent with the angular measurement between equivalent <210> textural maxima in Fig. 11b, where white and black triangles define an angle of 152°. The proposed substrate induced twinning model reflects these observations as well as the features of celestite aggregates as shown in Fig. 6.

Conclusions

The interaction of anhydrite cleavage surfaces with Sr-bearing aqueous solutions leads to the dissolution of the primary anhydrite and the concomitant nucleation of 3D celestite nuclei according to the Volmer Weber epitaxial growth mechanism. The structural matching between the anhydrite substrate and the celestite overgrowth determines the epitactic nature of the latter.

Two textural components have been identified in celestite aggregates growing on $(100)_{\text{Anh}}$ and $(001)_{\text{Anh}}$. These components represent the endmembers of the progressive development of celestite epitactic growth on anhydrite planes, and correlate with the following symmetry elements that belong to the anhydrite substrate:

- On $(100)_{\mathrm{Anh}}$, component A shows celestite crystals with an initial orientation of $(001)_{\mathrm{Clt}}$ parallel to $(100)_{\mathrm{Anh}}$ and $<120>_{\mathrm{Clt}}$ parallel to $[001]_{\mathrm{Anh}}$ and $[010]_{\mathrm{Anh}}$. They correlate with the 4-fold twinned crystals, whose constituting subunits rotate from $(001)_{\mathrm{Clt}}$ parallel to $(100)_{\mathrm{Anh}}$ to ±50° around *Y*-axis (*i.e.* $//[001]_{\mathrm{Anh}}$). Component B is the result of a rotation of crystal subunit oriented with $(001)_{\mathrm{Clt}}$ parallel to $(001)_{\mathrm{Anh}}$, and $(210)_{\mathrm{Clt}}$ parallel to $(100)_{\mathrm{Anh}}$ up to ±30° around the *X*-axis.

- On $(001)_{\mathrm{Anh}}$, component A is represented by celestite crystals primary oriented with $(001)_{\mathrm{Clt}}$ parallel to $(100)_{\mathrm{Anh}}$, and $(210)_{\mathrm{Clt}}$ parallel to $(001)_{\mathrm{Anh}}$. Component B is generated by progressive misorientation of celestite subunits, with an accumulated rotation of ±70° around an $<hk0>_{\mathrm{Clt}}$ axis (*e.g.* <210>), approximately aligned to *X*-axis. The celestite aggregates that result from this progressive subunit misorientation show a characteristic swan-like habit. In parallel, geometrical relationships have been identified which are consisting with the development of substrate induced twinning, with the mirror plane $(010)_{\mathrm{Anh}}$ acting as the twin plane after coalescence of differently oriented swan-like aggregates.

The strongest texture (F^2-index) is recorded on $(100)_{\mathrm{Anh}}$, followed by that on $(001)_{\mathrm{Anh}}$. Texture strength inversely correlates with the relative number of celestite crystals randomly oriented, where $(001)_{\mathrm{Anh}}$ shows the largest number of crystals with a random orientation (0.48 m.r.d.). Celestite texture on sample $(010)_{\mathrm{Anh}}$ is consistent with it, resulting from a mixture of the textural components derived from celestite overgrowths on step and edge pits, where $(100)_{\mathrm{Ahn}}$ and $(001)_{\mathrm{Anh}}$ are exposed. Consequently, the development of this texture is not related to epitactic growth on $(010)_{\mathrm{Anh}}$ but on $(100)_{\mathrm{Ahn}}$ and $(001)_{\mathrm{Anh}}$.

We attribute the development of the misorientational spreads involved in the formation of celestite aggregates on anhydrite substrates to split growth phenomena induced by incorporation of small amounts of Ca substituting Sr in celestite structure. This incorporation would induce lattice strain which would be released through the formation of dislocations spatially arranged at regular intervals in small-angle boundaries. The anisotropic development of misorientational spreads observed in the swan-like celestite aggregates formed on (001) anhydrite substrate could be due to differences in the amount of Ca incorporated in different regions of celestite crystals depending on their relative proximity to the anhydrite substrate and driven by the existence of compositional gradients at the boundary layer. The coalescence of differently oriented 3D celestite crystals on anhydrite cleavage surfaces generates microporosity within the secondary celestite layer. This porosity guarantees that, despite the existence of epitactic relationships between the celestite and the anhydrite, the transformation reaction can proceed.

Conflicts of interest

There are no conflicts to declare.

Acknowledgements

This study was supported by the MINECO (Spain) under project CGL2016-77138-C2-1-P. PF acknowledges a FPU predoctoral-contract (FPU17/01689) from the Spanish Ministry of Science, Innovation and Universities. PF, JMA and LFD are greatful to Ana Vicente, Miriam García, Ángel Mazarío (CNME) and Ignacio Carabias (CAI Rayos X, UCM) for providing excellent assistance. JGB appreciates financial support by the Spanish Ministry of Science and Innovation through the IEDI-2016-00691 fellowship and the project CGL2016-78560-P of the Spanish Ministry of Economy, Industry and Competitiveness. We acknowledge the European Synchrotron Radiation Facility (ESRF) for provision of synchrotron radiation facilities (Experiment number ES-698) and we would like to thank Carlotta Giacobbe for providing superb assistance in using beamline ID11.

References

1 K. W. Kolasinski, *Surface Science: Foundations of Catalisys and Nanoscience*, John Willey Sons, Ltd, England, 2002, p. 305.

2 S. Wagner, Epitaxy in solar cells, *J. Cryst. Growth*, 1975, **31**, 113–121.

3 A. Altree-Williams, A. Pring, Y. Ngothai and J. Brugger, Textural and compositional complexities resulting from coupled dissolution–reprecipitation reactions in geomaterials, *Earth-Sci. Rev.*, 2015, **150**, 628–651.

4 L. A. Casella, E. Griesshaber, X. Yin, A. Ziegler, V. Mavromatis, D. Müller, A. C. Ritter, D. Hippler, E. M. Harper, M. Dietzel, A. Immenhauser, B. R. Schöne, L. Angiolini and W. W. Schmahl, Experimental diagenesis: insights into aragonite to calcite transformation of Arctica islandica shells by hydrothermal treatment, *Biogeosciences*, 2017, **14**, 1461–1492.

5 J. S. Gill and G. H. Nancollas, The growth of gypsum crystals on barite and calcite, *Desalination*, 1979, **29**, 247–254.

6 C. Perdikouri, A. Kasioptas, T. Geisler, B. C. Schmidt and A. Putnis, Experimental study of the aragonite to calcite transition in aqueous solution, *Geochim. Cosmochim. Acta*, 2011, **75**, 6211–6224.

7 C. Perdikouri, S. Piazolo, A. Kasioptas, B. C. Schmidt and A. Putnis, Hydrothermal replacement of aragonite by calcite: interplay between replacement, fracturing and growth, *Eur. J. Mineral.*, 2013, **25**, 123–136.

8 Y. Zhang and D. Xue, In situ micro-Raman spectroscopy of gypsum crystallization driven by chemical reaction, *J. Mol. Struct.*, 2020, 128043.

9 A. Putnis, *Introduction to Mineral Sciences*, Cambridge University Press, 1992, p. 457.

10 R. G. J. Strens, Stability of Al_2SiO_5 solid solutions, *Mineral. Mag.*, 1968, **36**, 839–849.

11 C. Pérez-Garrido, L. Fernández-Díaz, C. M. Pina and M. Prieto, In situ AFM observations of the interaction between calcite (1014) surfaces and Cd-bearing aqueous solutions, *Surf. Sci.*, 2007, **601**, 5499–5509.

12 C. Pérez-Garrido, J. M. Astilleros, L. Fernández-Díaz and M. Prieto, In situ AFM study of the interaction between calcite {1014} surfaces and supersaturated Mn^{2+}–CO_3^{2-} aqueous solutions, *J. Cryst. Growth*, 2009, **311**, 4730–4739.

13 M. Prieto, P. Cubillas and Á. Fernández-Gonzalez, Uptake of dissolved Cd by biogenic and abiogenic aragonite: a comparison with sorption onto calcite, *Geochim. Cosmochim. Acta*, 2003, **67**, 3859–3869.

14 T. Roncal-Herrero, J. M. Astilleros, P. Bots, J. D. Rodríguez-Blanco, M. Prieto, L. G. Benning and L. Fernández-Díaz, Reaction pathways and textural aspects of the replacement of anhydrite by calcite at 25 °C, *Am. Mineral.*, 2017, **102**, 1270–1278.

15 A. Godelitsas and J. M. Astilleros Dissolution, sorption/(re) precipitation, formation of solid solutions and crystal growth phenomena on mineral surfaces: implications for the removal of toxic metals from the environment, in *Ion Partitioning in Ambient-Temperature Aqueous Systems*, ed. M. Prieto and H. Stoll, Mineralogical Society of Great Britain and Ireland, London, 2010, pp. 289–324.

16 I. Cuesta Mayorga, J. M. Astilleros, L. Fernández-Díaz, J. Morales, M. Prieto, T. Roncal-Herrero and L. G. Benning, Epitactic overgrowths of calcite ($CaCO_3$) on anhydrite ($CaSO_4$) cleavage surfaces, *Cryst. Growth Des.*, 2018, **18**, 1666–1675.

17 A. A. Chernov, Nucleation and epitaxy, in *Modern Crystallographic III: Crystal Growth; Springer Series on Solid-State Science 36*, Springer-Verlag, Berlin, 1984, pp. 48–103.

18 J. H. Van der Merwe, Equilibrium structure of a thin epitaxial film, *J. Appl. Phys.*, 1970, **41**, 4725–4731.

19 J. H. Van Der Merwe, The role of lattice misfit in epitaxy, *Crit. Rev. Solid State Mater. Sci.*, 1978, **7**, 209–231.

20 M. Copel, M. C. Reuter, E. Kaxiras and R. M. Tromp, Surfactants in epitaxial growth, *Phys. Rev. Lett.*, 1989, **63**, 632.

21 M. M. R. Evans, J. C. Glueckstein and J. Nogami, Epitaxial growth of manganese on silicon: Volmer-Weber growth on the Si (111) surface, *Phys. Rev. A: At., Mol., Opt. Phys.*, 1996, **53**, 4000.

22 P. Müller, A. Fach, J. John, A. N. Tiwari, H. Zogg and G. Kostorz, Structure of epitaxial PbSe grown on Si (111) and Si (100) without a fluoride buffer layer, *J. Appl. Phys.*, 1996, **79**, 1911–1916.

23 J. Morales, J. M. Astilleros, L. Fernández-Díaz, P. Álvarez-Lloret and A. Jiménez, Anglesite ($PbSO_4$) epitactic overgrowths and substrate-induced twinning on anhydrite ($CaSO_4$) cleavage surfaces, *J. Cryst. Growth*, 2013, **380**, 130–137.

24 I. Sunagawa, *Crystals: Growth, Morphology, Perfection*, Cambridge University Press, Cambridge, 2005, p. 295.

25 I. Sethmann, J. Wang, U. Becker and A. Putnis, Strain-induced segmentation of magnesian calcite thin films growing on a calcite substrate, *Cryst. Growth Des.*, 2010, **10**, 4319–4326.

26 R. People and J. C. Bean, Calculation of critical layer thickness versus lattice mismatch for Ge_xSi_{1-x}/Si strained-layer heterostructures, *Appl. Phys. Lett.*, 2010, **47**, 322–324.

27 W. A. Tiller, *The Science of Crystallization: Microscopic Interfacial Phenomena*, Cambridge University Press, 1991, p. 391.

28 B. W. Dodson and J. Y. Tsao, Relaxation of strained-layer semiconductor structures via plastic flow, *Appl. Phys. Lett.*, 1987, **51**, 1325–1327.

29 P. M. J. Marée, J. C. Barbour, J. F. Van der Veen, K. L. Kavanagh, C. W. T. Bulle-Lieuwma and M. P. A. Viegers, Generation of misfit dislocations in semiconductors, *J. Appl. Phys.*, 1987, **62**, 4413–4420.

30 R. Hull and J. C. Bean, Misfit dislocations in lattice-mismatched epitaxial films, *Crit. Rev. Solid State Mater. Sci.*, 1992, **17**, 507–546.

31 L. Fernández-Díaz, J. M. Astilleros and C. M. Pina, The morphology of calcite crystals grown in a porous medium doped with divalent cations, *Chem. Geol.*, 2006, **225**, 314–321.

32 K. Sangwal, *Etching of crystals: theory, experiment and application*, Elsevier, 2012.

33 J. M. Astilleros, L. Fernández-Díaz and A. Putnis, The role of magnesium in the growth of calcite: An AFM study, *Chem. Geol.*, 2010, **271**, 52–58.

34 R. H. Mitchell, M. I. Novgorodova and E. I. Semenov, Chemical Composition of Minerals, Crystallochemical Constraints and the Nature of Impurities, in *Advanced Mineralogy*, ed. A. S. Marfunin, Springer, Berlin, Heidelberg, 1994.

35 Á. Fernández-González, M. Prieto, A. Putnis and S. López-Andrés, Concentric zoning patterns in crystallizing (Cd,Ca)CO_3 solid solutions from aqueous solutions, *Mineral. Mag.*, 1999, **63**, 331–343.

36 N. Sánchez-Pastor, C. M. Pina, J. M. Astilleros, L. Fernández-Díaz and A. Putnis, Epitaxial growth of celestite on barite (001) face at a molecular scale, *Surf. Sci.*, 2005, **581**, 225–235.

37 N. Sánchez-Pastor, C. M. Pina and L. Fernández-Díaz, Relationships between crystal morphology and composition in the (Ba,Sr)SO_4–H_2O solid solution–aqueous solution system, *Chem. Geol.*, 2006, **225**, 266–277.

38 U.S. Geological Survey, *Mineral Commodity Summaries*, 2003, pp. 162–163, https://s3-us-west-2.amazonaws.com/prd-wret/assets/palladium/production/mineral-pubs/mcs/mcs2003.pdf.

39 J. S. Hanor, A model for the origin of large carbonate-and evaporite-hosted celestine ($SrSO_4$) deposits, *J. Sediment. Res.*, 2004, **74**, 168–175.

40 A. Putnis, Mineral replacement reactions, *Rev. Mineral. Geochem.*, 2009, **70**, 87–124.

41 F. C. Hawthorne and R. B. Ferguson, Anhydrous sulphates; I, Refinement of the crystal structure of celestite with an appendix on the structure of thenardite, *Can. Mineral.*, 1975, **13**, 181–187.

42 F. C. Hawthorne and R. B. Ferguson, Anhydrous sulphates; II, Refinement of the crystal structure of anhydrite, *Can. Mineral.*, 1975, **13**, 289–292.

43 D. Palmer, *Crystal Maker Crystal Maker Software Ltd Yarnton England*, 2005.

44 J. G. Gómez-Barreiro, H. R. Wenk and S. Vogel, Texture and elastic anisotropy of a mylonitic anorthosite from the Morin Shear Zone (Quebec, Canada), *J. Struct. Geol.*, 2015, **71**, 100–111.

45 A. P. Hammersley, S. O. Svensson and A. Thompson, Calibration and correction of spatial distortions in 2D detector systems, *Nucl. Instrum. Methods Phys. Res., Sect. A*, 1994, **346**, 312–321.

46 L. Lutterotti, S. Matthies, H. R. Wenk, A. S. Schultz and J. J. W. Richardson, Combined texture and structure analysis of deformed limestone from time-of-flight neutron diffraction spectra, *J. Appl. Phys.*, 1997, **81**, 594–600.

47 F. C. Hawthorne and R. B. Ferguson, Anhydrous sulphates; I, Refinement of the crystal structure of celestite with an appendix on the structure of thenardite, *Can. Mineral.*, 1975, **13**, 181–187.

48 S. Matthies and G. W. Vinel, On the reproduction of the orientation distribution function of texturized samples from reduced pole figures using the conception of a conditional ghost correction, *Phys. Status Solidi B*, 1982, **112**, K111–K114.

49 H. R. Wenk, S. Matthies, J. Donovan and D. Chateigner, BEARTEX: a Windows-based program system for quantitative texture analysis, *J. Appl. Crystallogr.*, 1998, **31**, 262–269.

50 H. J. Bunge, *Texture analysis in materials science: mathematical methods*, Elsevier, 2013.

51 J. Gómez Barreiro, I. Lonardelli, H. R. Wenk, G. Dresen, E. Rybacki, Y. Ren and C. N. Tomé, Preferred orientation of anorthite deformed experimentally in Newtonian creep, *Earth Planet. Sci. Lett.*, 2007, **264**, 188–207.

52 L. Lutterotti, R. Vasin and H. R. Wenk, Rietveld texture analysis from synchrotron diffraction images. I. Calibration and basic analysis, *Powder Diffr.*, 2014, **29**, 76–84.

53 H. R. Wenk, L. Lutterotti, P. Kaercher, W. Kanitpanyacharoen, L. Miyagi and R. Vasin, Rietveld texture analysis from synchrotron diffraction images. II. Complex multiphase materials and diamond anvil cell experiments, *Powder Diffr.*, 2014, **29**, 220–232.

54 H. Shindo, K. Shitagami, S. Kondo and A. Seo, Atomic force microscopic observation of directional layer growth and dissolution on surfaces of sulfate minerals, *J. Cryst. Growth*, 1999, **198**, 253–257.

55 M. Prieto, A. Putnis, L. Fernández-Díaz and S. López-Andrés, Metastability in diffusing-reacting systems, *J. Cryst. Growth*, 1994, **142**(1–2), 225–235.

56 A. Putnis, M. Prieto and L. Fernandez-Diaz, Fluid supersaturation and crystallization in porous media, *Geol. Mag.*, 1995, **132**(1), 1–13.

57 A. Putnis, Transient porosity resulting from fluid–mineral interaction and its consequences, *Rev. Mineral. Geochem.*, 2015, **80**, 1–23.

58 I. Kostov and R. I. Kostov, *Crystal habits of minerals. Bulgarian Academic Monographs (1)*, Pensoft Publishers and Prof. Marin Drinov Academic Publishing House, 1999.

59 P. Hartman and C. S. Strom, Structural morphology of crystals with the barite ($BaSO_4$) structure: a revision and extension, *J. Cryst. Growth*, 1989, **97**, 502–512.

60 F. R. Massaro, L. Pastero, E. Costa, G. Sgualdino and D. Aquilano, Single and Twinned Li_2CO_3 Crystals (Zabuyelite) Epitaxially Grown on {0001} and {1014} Forms of $CaCO_3$ (Calcite) Crystals, *Cryst. Growth Des.*, 2008, **8**, 2041–2046.

61 A. G. Shtukenberg, J. M. Astilleros and A. Putnis, Nanoscale observations of the epitaxial growth of hashemite on barite (001), *Surf. Sci.*, 2005, **590**, 212–223.

62 A. J. Pinto, A. Jimenez and M. Prieto, Interaction of phosphate-bearing solutions with gypsum: Epitaxy and induced twinning of brushite ($CaHPO_4 \cdot 2H_2O$) on the gypsum cleavage surface, *Am. Mineral.*, 2009, **94**, 313–322.

63 D. Hull and D. J. Bacon, *Introduction to dislocations*, Elsevier, 2011, vol. 37.

64 F. Nindiyasari, E. Griesshaber, L. Fernandez-Diaz, J. M. Astilleros, N. Sanchez-Pastor, A. Ziegler and W. W. Schmahl, Effects of Mg and hydrogel solid content on the crystallization of calcium carbonate in biomimetic counter-diffusion systems, *Cryst. Growth Des.*, 2014, **14**, 4790–4802.

65 F. Nindiyasari, L. Fernández-Díaz, X. Yin, M. Greiner, E. Griesshaber, M. Tsige, A. Ziegler and W. W. Schmahl, Influence of gel-strength and magnesium doping on the organization of calcite/hydrogel mesocrystal composites, *Eur. J. Mineral.*, 2019, **31**, 217–229.

66 C. V. Putnis, K. Tsukamoto and Y. Nishimura, Direct observations of pseudomorphism: compositional and textural evolution at a fluid-solid interface, *Am. Mineral.*, 2005, **90**, 1909–1912.

67 E. Ruiz-Agudo, C. V. Putnis and A. Putnis, Coupled dissolution and precipitation at mineral–fluid interfaces, *Chem. Geol.*, 2014, **383**, 132–146.

68 E. Ruiz-Agudo, H. E. King, L. D. Patiño-López, C. V. Putnis, T. Geisler, C. Rodriguez-Navarro and A. Putnis, Control of silicate weathering by interface-coupled dissolution-precipitation processes at the mineral-solution interface, *Geology*, 2016, **44**, 567–570.

69 P. Forjanes, J. M. Astilleros and L. Fernández-Díaz, The Formation of Barite and Celestite through the Replacement of Gypsum, *Minerals*, 2020, **10**(2), 189.

70 R. W. Allmendinger, N. Cardozo and D. M. Fisher, *Structural geology algorithms: Vectors and tensors*, Cambridge University Press, 2011, p. 286.